Factorial-Based Response Surfaces With Confidence Intervals for Optimizing Thermal-Optical Analysis of Atmospheric Black Carbon

J.M. Conny*, Surface and Microanalysis Science Division, National Institute of Standards and Technology, 100 Bureau Drive Stop 8372, Gaithersburg, MD 20899

G.A. Norris, National Exposure Research Laboratory, U.S. Environmental Protection Agency, Research Triangle Park, NC

T.R. Gould, Dept. of Civil and Environmental Engineering, University of Washington, Seattle, WA

* Author to whom correspondence should be sent.

ABSTRACT

We demonstrate how thermal-optical transmission analysis (TOT) for refractory light-absorbing carbon in atmospheric particulate matter was optimized with empirical response surface modeling. TOT employs pyrolysis to distinguish the mass of black carbon (BC) from organic carbon (OC); however, it does not physically separate them. The optimization compared response surfaces for the cross sections, which revealed the effects of varying instrument conditions, in particular, the high-temperature pyrolysis step in helium. Models were derived from a central composite factorial measurement design with three factors: temperature and duration of the high-temperature pyrolysis step, and the extent that heating increased in the oxidizing phase. The response surface for the apparent specific absorption cross section of original BC, as determined by the instrument (σ_{BC}), revealed a ridge that indicated the thermal conditions for sufficient pyrolysis of OC. The intersection of σ_{BC} and the apparent specific absorption cross section for pyrolyzed OC (σ_{Char}) indicated the conditions where the cross sections were equivalent. The intersection of the 95 % confidence interval surfaces for σ_{Char} with the σ_{BC} surface defined a confidence region for a range of pyrolysis temperatures and durations.

INTRODUCTION

Atmospheric particulate matter (PM) associated with incomplete combustion adversely affects human health[1;2], visibility[3;4], and impacts Earth's radiative balance[5-7]. For measuring the mass of refractory carbon from combustion, i.e., elemental carbon (EC) in PM <2.5 μm, the U.S. EPA employs thermal-optical analysis (TOA) in its National Air Monitoring System. To quantify EC and distinguish it from organic carbon (OC), TOA combines a temperature protocol for removing carbonaceous material on a particle-laden quartz fiber filter with a system to optically monitor the production of pyrolyzed OC on the filter during heating[8;9]. The optical part of TOA for the thermal-optical transmission method (TOT) in particular implies that what is measured is the mass of the light-absorbing component of EC, i.e., black carbon (BC). However, TOA is problematic in that different temperature protocols produce different results for BC on the same sample material[10;11], and established protocols have been shown to produce BC measurements that disagree substantially with other methods[12-14].

Figure 1 is a schematic of the TOT instrument and an example of its thermogram. During the first stage of TOT analysis that typically employs four heating steps in an inert (helium) atmosphere within the front oven, thermally unstable OC is pyrolyzed, which causes the attenuation of laser light (670 nm) through the filter. Thermally stable OC is also removed from the filter at this stage and measured by flame ionization detection (FID). Later, in an oxidizing atmosphere of 1 % to 2 % O_2 in He in the front oven, pyrolyzed OC as well as the native BC (i.e., original BC) in the sample are removed from the filter and measured by FID. With the removal of light-absorbing carbon, the laser signal returns to the point prior to OC pyrolysis (split point). All carbon beyond this point is quantitatively assigned to BC, while all carbon

measured prior to this point is quantitatively assigned to OC. The split point does not, however, physically separate OC from native BC[15;16]. For TOT to accurately determine BC mass based on the Beer-Lambert Law, pyrolyzed OC and BC must have the same optical absorption properties[16;17].

Several radiative transfer models have been applied to methods that measure light-absorbing PM bound to a fibrous filter[18-21] including one to TOA[21]. Nevertheless, a reliable physical model for determining the TOT temperature protocol for measuring Beer-Lambert mass remains elusive because of the complexity of pyrolysis product formation on quartz fibers[22] and differences in the optical behavior of pyrolyzed OC vs. BC for different types of samples. As an alternative to radiative transfer modeling for optimizing the temperature protocol, we demonstrate the use of empirical response-surface modeling.

Response surfaces are polynomial-based empirical models of predictable systems that are commonly interpreted graphically[23;24]. In chemical analysis, they are powerful tools for predicting how an instrument will perform when multiple adjustable parameters are involved in generating the instrument response[25]. In effect, response surface models allow us to study the behavior of an instrument graphically from 3-dimensional representations of the response as a function of variation in the instrument parameters.

Previously our NIST lab demonstrated the effects of two principal sources of bias in TOT[10]. First, inadequate pyrolysis of OC due to insufficient heating during the critical step in He (step 4) results in a positive bias when residual unpyrolyzed OC is measured beyond the split point as native BC. Among thermal oxidation methods, OC may be overestimated as much as a factor of 50 if OC is carried into the fraction of refractory carbon[26]. Second, any loss of pyrolyzed OC or

native BC during step 4 in He, which is not accounted for by the laser signal, results in a negative bias. The current study also considers these biases; however, we now model the optical behavior of pyrolyzed OC and native BC as separate optical components from their specific absorption cross sections. We demonstrate how the superposition of response surfaces for the cross sections is used to adjust the temperature and duration of the step in He such that the cross sections are equivalent. Moreover, confidence intervals for the response surfaces reveal the range of acceptable pyrolysis conditions in He.

METHODS

Models were based on PM2.5 samples collected on heat-purified 20 cm x 25 cm quartz fiber filters using an MSP Universal Air Sampler during February 23, 2005 to March 10, 2005 in a residential section of Seattle, WA. Analyses suggest that the samples contained woodburning emissions, presumably from residential heating[27]. Ancillary samples were collected during late fall 2004 from the Los Angeles, CA PM Supersite near the University of Southern California and during late summer 2004 from a light industrial section of Atlanta, GA. Details of the sampling operation are reported elsewhere[27;28]. All TOT measurements were made with Sunset Laboratory's Dual-Optics Thermal Carbon Analyzer[†]. Quality control samples were run using standards of sucrose or urea. Controls showed that within-day FID drift occurred (Fig. S1); however, all recoveries with one exception were within 6 % (exception was 13 %), and drift was independent of the standard or carbon level.

[†] Commercial products identified in this document specify the means by which experiments were conducted. Such identification is not intended to imply recommendation or endorsement by NIST or by EPA nor is it intended that the identified products are necessarily the best available for the purpose.

Response Surface Modeling

In this study, response surface models were constructed to accommodate three factors from the TOT method: 1) He step-4 temperature, 2) He step-4 duration, 3) temperature step ramp in the O_2-He phase. The model that best determined the main factor effects, self interactions, and between-factor interactions for the three factors is a full second-order polynomial[24;25;29] with 10 terms plus random error:

$$y_{1i} = \beta_0 + \beta_1 x_{1i} + \beta_2 x_{2i} + \beta_3 x_{3i} + \ldots \quad \text{main effects}$$
$$\beta_{11} x_{1i}^2 + \beta_{22} x_{2i}^2 + \beta_{33} x_{3i}^2 + \ldots \quad \text{self interactions}$$
$$\beta_{12} x_{1i} x_{2i} + \beta_{13} x_{1i} x_{3i} + \beta_{23} x_{2i} x_{3i} + e_{1i} \quad \text{between-factor interactions} \quad (1)$$

Here, y_{1i} is the modeled response for experiment i; β_0, β_1, β_2, … are the model parameters; x_{1i}, x_{2i}, x_{3i} are the factor values for experiment i. Estimates of the model parameters (β) are calculated from matrix inversion. Here, b is the vector of parameter estimates, X is the matrix of factor values associated with the two measurement levels, and y is the vector of measured response values:

$$b = (X'X)^{-1}(X'y) \quad (2)$$

Measured responses were assumed to be non-correlated and, thus, independent. The assumption is appropriate because the process of adjusting the TOT temperature protocol to establish factor levels did not affect the other factors. For example, establishing the He step-4 temperatures required no manipulation of step-4 duration or the temperature ramps in the O_2-He phase.

Apparent Specific Absorption Cross Sections

Laser transmission signals were log-transformed to an attenuation time series ($ATN(t)$) using the version of the Beer-Lambert Law that has been applied to the Aethalometer[30;31]:

$$ATN(t) = -100 \ln\left(\frac{I(t)}{I_0}\right) \quad (3)$$

Here, $I(t)$ is the transmission signal time series. I_0 was taken at the end of the run after all carbon has been removed from the filter and then corrected to the TOT starting temperature (40 °C to 50 °C) based on laser signal differences at low and high temperatures for clean filters.

A follow-up TOT run after all carbon had been removed revealed a modest but consistent attenuation with increasing heat that was due to residual refractory non-carbonaceous material on the filter. Attenuation from the follow-up run was, therefore, used as a blank ($ATN(t)_B$) with the attenuation due to all labile and oxidizable (mainly carbon) material, $ATN(t)_L$, determined from:

$$ATN(t)_L = ATN(t) - ATN(t)_B \quad (4)$$

It was assumed that by step 4 in He all light-scattering OC had been either volatilized or pyrolyzed to highly-absorbing carbonaceous material and from this point through the O_2-He phase, $ATN(t)_L$ was largely due to attenuation by carbon. Backscattering by refractory carbon at this point was assumed to be minimal because in a thinly-loaded diffusely reflective substrate, forward scattering largely cancels backscattering[18;32]. Any residual attenuation[33] by non-carbonaceous material was corrected by the blank. ATN_C is denoted as the value of $ATN(t)_L$ at maximum charring during step 4 in He. Following Petzold et al.[34], ATN_C is equal to the product of the specific carbon mass loading (S_C, mg C cm^{-2}) and the specific attenuation cross section due to carbon alone (σ_C, m^2 g^{-1}):

$$ATN_C = \sigma_C S_C \quad (5)$$

Here, it is assumed that ATN_C is associated principally with absorption. At the point of maximum charring in the He phase, ATN_C is the sum of the attenuation due to charring (ATN_{Char}) and the attenuation due to native BC in the sample (ATN_{BC}):

$$ATN_C = ATN_{Char} + ATN_{BC} \quad (6)$$

Here, ATN_{Char} is calculated as in Eqs. 3-5; however, I_0 in this case is taken at the *beginning* of the TOT run prior to the start of thermal desorption rather than at the end of the run after all carbon has been removed. I_0 in this case includes absorption due to native BC, which effectively factors out native BC from ATN_{Char} (Eq. 3). ATN_{BC} is determined by difference in Eq. 6. We now express ATN_{Char} and ATN_{BC} as the products of their respective specific absorption cross sections and carbon mass loadings (μg C cm^{-2}):

$$ATN_{Char} = \sigma_{Char} S_{Char} \quad (7)$$

$$ATN_{BC} = \sigma_{BC} S_{BC} \quad (8)$$

Here, S_{BC} is the mass loading remaining at the split point, and S_{Char} is equal to S_C at the point of maximum charring less S_{BC}. Due to absorption enhancement from multiple scattering[32;35;36] and other potential differences in the optical behavior of pyrolyzed OC vs. native BC[22], σ is referred to here as the *apparent* TOT specific absorption cross section. Importantly, σ_{BC} is a method-dependent property (like σ_{Char}), rather than an absolute property of the original BC. σ_{BC} necessarily varies with the instrument's temperature protocol and can, thus, be modeled. As we

show below, it is the relationship between σ_{BC} and σ_{Char} models that allows us to determine optimal TOT conditions.

Factorial Experimental Design

The orthogonal and rotatable central composite factorial design[29] used here combines a two-level full factorial with a two-level partial (star) factorial design (Fig. 2). To estimate the 10 model parameters from the set of simultaneous equations represented in Eq. 1, the factorial design must have at least 10 factor combinations at which y determinations are made. The central composite design required 15 factor combinations. Thus, the design required only a small surplus of factor combinations (5) over the minimum needed for generating a full 2nd order response surface, making the design highly efficient for this purpose.

Table 1 shows the instrument conditions for Factors 1 and 2. For Factor 1, temperature of He step 4 ranged from 630 °C to 890 °C with the design center point at 760 °C. For Factor 2, duration of step-4 in He ranged from 60 s to 270 s, with the design center point at 165 s. Since we previously showed that variation in He steps 1-3 do not significantly affect the BC/total carbon ratio (BC/TC) in TOT[10], these steps were fixed at 200 °C, 400 °C, and 600 °C, respectively, for 60 s.

Table 1. Instrument Conditions for Factors 1 and 2 in the Central Composite Design

For Factor 3, variation in step temperatures in the O_2-He phase was established as a series of five

	Star Factorial Lower Level	Full Factorial Lower Level	Star Factorial Middle Level	Full Factorial Upper Level	Star Factorial Upper Level
Factor 1: He Step-4 Temperature (°C)	630	668	760	852	890
Factor 2: He Step-4 Duration (s)	60	91	165	239	270

temperature step ramps (indicated by their initial temperatures) as shown in Fig. 3. Factor 3 was designed such that the design center had 550 °C as its initial temperature. The temperature of the final (6^{th}) step was held constant at 900 °C, and steps 2-5 were adjusted accordingly so that the step-to-step rise was linear among the different factorial levels. Durations of the O_2-He steps were fixed at 60 s, 60 s, 45 s, 45 s, 45 s, and 90 s, respectively.

Three-Day Measurement Protocol

In addition to measurements at the 15 sets of instrument conditions in the factorial design (Fig. 2), nine additional measurements were used as replicates for each sample. A follow-up TOT run was also made as a blank for each of the 24 measurements. The total of 48 runs on each sample required three days to complete, which placed special demands on the design to avoid the effect of systematic error. To meet these demands, a blocked, replicated, and randomized scheme for each day's runs was developed as shown in Figure 4. The purpose was to distribute the sets of instrument conditions such that the whole factor space was adequately assessed each day and that day-to-day variation in instrument behavior would not impart systematic error in the response surface models. Eight measurement runs (and 8 blank runs) were made on each day as shown in Fig. 4. Replication of key points in the design insured that any confounding of the models by within-day instrument drift or day-to-day variation could be tested.

Confidence Intervals for Response Surface Models

Surface confidence intervals were important in this study for revealing the range of acceptable TOT temperatures and durations. Confidence intervals were calculated from Deming and Morgan[24] as follows:

$$\hat{y}_{CI} = \hat{y} \pm \sqrt{\{F_{(1,n-p)} s_r^2 (1 + [X_0 (X'X)^{-1} X'_0])\}} \quad (9)$$

Here, $\hat{y}$ is the estimate of the response from the model, $F_{(1,n-p)}$ is the F-statistic based on n experiments and a model with p parameters, s_r^2 is the model variance based on model residuals determined from replicated measurements, X is a matrix of coefficients associated with the model parameters (Eq. 1), and X_0 is a related matrix of coefficients associated with each factorial combination. X contains additional redundant coefficients to account for experiments that were replications in the design.

Response surface confidence intervals reflect uncertainty associated with the spacing of levels in the factorial design as well as the residuals in the response variable. For example, if factor levels represented by the star in Fig. 2 extend far beyond the levels of the full factorial, confidence interval surfaces will tend to exhibit excessive and distorted error at the edges of the response model space. To minimize this distortion, star factorial levels are adjusted such that their magnitudes are comparable with the full factorial levels. This is accomplished by making the design rotatable as shown in Fig. 5.

Figure 5 also shows that the distance between the center point and its nearest neighbor is larger than the distance between all other points and their remaining neighbors. The result is that the response surface tends to have more uncertainty at the center of the model space. This center-point uncertainty causes an anomalous "bulging" of the confidence surfaces at the center of the model space (Fig. S2a). The uncertainty artifact is corrected by making replicate measurements at the design center (Fig. S2b).

RESULTS AND DISCUSSION

Veracity of Experimental Design

To test if significant measurement drift occurred during the three days of measurements for each sample, we compared the within-day variance and between-day variance in BC measurements using the thermal protocol associated with design center point (Table 1, Fig. 3). First, however, we verified that the measurements were normally distributed (Fig. S3). This was accomplished using the six within-day duplicate measurements in the three-day measurement protocol (points with concentric circles in Fig. 4). The approach was appropriate because the BC duplicate differences were independent of the actual BC levels and, thus were expected to form a single distribution.

Table 1 shows results of the analysis of BC measurement variance for two samples from Seattle along with ancillary samples from Atlanta and Los Angeles. Within-day variation is used to test if any systematic error was related to the type of factorial combination in the design, i.e., center point vs. peripheral points. For all samples, the within-day F-value (col. 5) is substantially smaller than the critical F-value with 95 % confidence (9.29), indicating that no significant systematic error is associated with the type of factorial combination. Moreover, any instrument drift during an analysis day did not translate to a BC measurement bias.

Table 1. Analysis of Variance from TOT BC Measurements

	Within-Day Variation				Between-Day Variation	Within-Day vs. Between-Day
	Center Variance[1] (df=3)[2]	Periphery Variance (df=3)	Center Plus Periphery Variance (df=5)	Center vs. Periphery *F*-test ($F_{0.95}$=9.28)	Center Variance (df=5)	Center *F*-test ($F_{0.95}$=5.05)
Atlanta #1	2.36E-04	4.32E-04	4.01E-04	1.83	2.47E-04	1.62
Atlanta #2	1.27E-02	1.29E-02	1.54E-02	1.02	8.83E-03	1.75
LA #1	3.56E-03	1.21E-03	2.86E-03	2.95	2.21E-03	1.30
LA #2	1.37E-02	1.53E-02	1.74E-02	1.12	9.40E-03	1.85
Seattle #1	3.22E-03	1.08E-03	2.58E-03	2.98	2.14E-03	1.21
Seattle #2	2.88E-03	1.00E-02	7.74E-03	3.48	1.73E-03	4.47

[1] ($\mu g\ C\ cm^{-2}$)[2]

[2] df=degrees of freedom

The between-day variation in Table 1 was used to test if there was an overall shift in TOT behavior during the entire three-day analysis period. Here only the center points were used. Comparing within-day vs. between-day variance, the *F*-value is again substantially smaller than the critical *F*-value with 95 % confidence (5.05), indicating no significant systematic measurement error associated with day-to-day TOT variation that might have confound the models.

BC/TC Measurements and Models

The two Seattle samples modeled in this study were collected for different durations (24 h and 48 h), which resulted in different levels of total carbon: 7.52 $\mu g\ cm^{-2}$ (level 1) and 12.9 $\mu g\ cm^{-2}$ (level 2). BC/TC determinations for all factor combinations in the experimental design are plotted in Fig. 6 with respect to He step-4 temperature (Factor 1) and He step-4 duration (Factor 2). The figure shows a fairly large decrease in BC/TC from 630 °C to 890 °C: 19 % for the level-1 sample and 24 % for the level-2 sample. This trend is consistent with a BC/TC decrease of 7 %

to 9 % per 100 °C increase in the step-4 temperature reported earlier for urban PM (NIST SRM 1649a)[10].

Figure 7 shows the modeled BC/TC response for the two samples as a function of the He step-4 temperature and duration. In this case, the 550 °C ramp (Fig. 3) was used for the O_2-He step temperature rise (Factor 3). At the low end of the temperature range, elevated BC/TC ratios are likely due to the positive artifact from the measurement of unpyrolyzed OC as native BC[10]. Over the upper half of the temperature range (760 °C to 890 °C), the BC/TC ratio for the level-2 sample clearly tends to level off while the ratio for the level-1 sample continues to exhibit a monotonic decrease. This contrast has also been observed in level-2 samples from the Los Angeles site[28]. The continued decrease in BC/TC at high temperatures in He for the level-1 sample is likely due to the effect of an oxidative loss of refractory carbon[10;15], to which the laser signal failed to adequately respond. By contrast, it appears that too much refractory carbon was present in the level-2 sample (72 % more than in the level-1 sample) for helium-phase oxidation to have had a noticeable affect.

Apparent Specific Absorption Cross Section Measurements and Models

Figure 8 shows that determinations of the apparent specific absorption cross sections for pyrolyzed OC and native BC both increased with the He step-4 temperature. The σ_{Char} increase with temperature was expected because increased heat not only pyrolyzed more carbon, but changed the absorptivity of the material as well. In Fig. 8 the σ_{Char} increase for the level-1 sample over the temperature range is twice as large as the overall σ_{BC} increase. The level-2 sample exhibited a similar trend.

Figure 9 shows the response surface models for σ_{Char} and σ_{BC} in the same plot. The overlay of models in this manner allows us to observe if an intersection of σ_{Char} and σ_{BC} surfaces exists, and therefore, the conditions under which σ_{Char} and σ_{BC} are equivalent. The level-1 sample clearly exhibits the intersection while the level-2 sample does not. In this comparison, the σ_{Char} determination (and model) for the level-2 sample is not reliable because the sample is overloaded with carbon. Among all samples (10) collected at the Seattle site, σ_{Char} determinations decrease dramatically, from 35 $m^2\ g^{-1}$ to 3.9 $m^2\ g^{-1}$, with increasing carbon loading (Fig. S4). The effect has been identified as the occluding of light, or shadowing, by an overabundance of particles in a fibrous matrix[33;37;38]. Since the level-2 sample is problematic because of this effect, we focus on the level-1 sample for determining the conditions for σ_{Char} and σ_{BC} equivalence ("Establishing Optimal TOT Step-4 Conditions" below).

σ_{Char} and σ_{BC} are, of course, related through Eqs. 6-8. Thus, if OC were overheated, i.e., overpyrolyzed, we might expect σ_{BC} to increase with σ_{Char} accordingly, since as mentioned earlier, pyrolyzed OC and the original BC do not physically separate at the split point. However, Fig. 9 clearly shows that these surfaces behave differently: σ_{Char} tends to be monotonic while σ_{BC} tends to be parabolic. The parabolic behavior of the σ_{BC} surface at higher step-4 temperatures also matches well the parabolic behavior of the BC/TC surface (Fig. 7b). At lower step-4 temperatures, σ_{BC} values are lower because of the presence of insufficiently pyrolyzed (and lower-absorbing) OC beyond the split point. The σ_{BC} surface forms a ridge at higher temperatures, which indicates the conditions where OC pyrolysis is sufficient. Rather than an indicator of the overpyrolysis of OC, the σ_{BC} surface indicates instead the presence of insufficiently pyrolyzed OC.

Figure 10 shows that the σ_{BC} surfaces for the two samples are remarkably similar. In fact, at temperatures above 760 °C the level-2 σ_{BC} surface is within the 95 % confidence intervals for the level-1 σ_{BC} surface. Furthermore, unlike the intersection of σ_{Char} and σ_{BC} surfaces, the σ_{BC} ridges for the two samples are remarkably close (see Fig. 12b). Thus, the conditions for sufficient OC pyrolysis are independent of the carbon level in the sample. This is important because ideally the TOT temperature protocol should be independent of carbon loading.

Effect of Factor 3

Adjusting the temperatures in the O_2-He phase may have the effect of shifting the relative positions at which pyrolyzed OC and native BC evolve in the thermogram. Figure 11 shows how σ_{Char} and σ_{BC} change with variation in the O_2-He temperature step ramp (Factor 3) for the level-1 sample. Little variation in σ_{Char} is seen, however, it appears that by increasing the ramp from 550 °C to 630 °C, σ_{BC} is substantially lowered at higher step-4 temperatures. The σ_{BC} surface ridge does not appear to change much with the O_2-He temperature ramp. However, because the σ_{BC} surface shifts lower rather than the σ_{Char} surface, we might expect the σ intersection to occur at lower He step-4 temperatures if, for example, the 630 °C O_2-He ramp is used rather than the 550 °C ramp. Nevertheless, Fig. 11 clearly shows that any shift in σ_{BC} caused by the O_2-He ramp is within the boundaries of the 95 % confidence intervals for the 550 °C ramp. Therefore, σ_{BC} variation with the O_2-He ramp does not appear to be statistically significant in our models, and from this sample alone we cannot determine with certainty how the σ_{Char} and σ_{BC} intersection might be affected by variation in the O_2-He ramp.

Establishing Optimal TOT Step-4 Conditions

An overhead view of superimposed σ_{Char} and σ_{BC} surfaces for the level-1 sample in Fig. 9 displays the functional nature of the surface intersection (Fig. 12a). We identify the optimal He step-4 conditions for this sample by projecting the surface intersection onto the time vs. temperature plane (Fig. 12b). The shaded area displays a confidence region bounded by the intersections of the σ_{Char} 95 % confidence intervals with the σ_{BC} surface. The σ_{BC} ridge for this sample is well within the confidence region. Fig. 12b also shows the σ_{BC} ridge and the BC/TC "trough" for the level-2 sample (Fig. 7), both of which are also well within the 95 % confidence region.

Even though the amount of carbon in the level-2 sample precludes us from establishing a σ intersection, there is excellent agreement among the σ intersection for the level-1 sample and the σ_{BC} ridges for the two samples. Clearly, from both the σ intersection and the σ_{BC} ridges, TOT optimization depends on the duration of step-4 in helium as well as the temperature, as reported by others[39]. Higher temperatures are allowed for a shorter duration. Selecting 150 s for the step-4 duration, a suitable temperature for the Seattle samples is around 830 °C to 850 °C. We do not, however, have sufficient reason to reject a temperature as low as 750 °C or as high as 890 °C for this duration since they are at the limits of the confidence region.

Our results are consistent with a relatively high step-4 temperature in protocols reported previously[10;40;41]. However, others have employed or suggested a much lower step-4 temperature for TOT[15;42]. The purpose of this study was to demonstrate the use of empirical modeling in TOT optimization. The treatment is based primarily on the analysis of samples from a single site. It is likely the response surface models of other site's samples that exhibit greater oxidative loss of

refractory carbon in the He phase (negative bias) would result in lower optimized step-4 temperatures[28]. A recommended comprehensive temperature protocol should be the product of a comparison of models and confidence regions for multiple sample types. Nevertheless, this study showed that the best conditions for the critical pyrolysis step in TOT are revealed graphically from the locations of the σ intersection and σ_{BC} ridges in empirical response surface models.

It is instructive to note that the sensitivity of response surface modeling to center-point replication in the central composite design described earlier had a bearing on the TOT optimization results. Distortion of the 95 % confidence surfaces (Fig. S2) caused the confidence region to widen and both the σ intersection and σ_{BC} ridge to shift to higher temperatures (Fig. S5). As a result, selection of a suitable He step-4 temperature would have been erroneously high.

CONCLUSION

We have demonstrated the use of empirical response surface models with confidence intervals for optimizing the temperature protocol for the TOT method based on the analysis of PM2.5 samples collected in Seattle, WA. An efficient central-composite factorial experimental design focusing on the temperature and duration of the critical high-temperature step in the helium phase (Factors 1 and 2) and the temperature step ramp in the O_2-He phase (Factor 3) was used for acquiring measurement data for the models. Models were full second-order polynomial surfaces exhibiting between-factor interaction as well as within-factor variation to reveal the optical absorption behavior of the TOT instrument. Since the number of measurements for the models required three analysis days and quality controls revealed drift in the FID response, bias in the models was critically avoided by randomizing the run order of the factorial conditions and

strategically using of replicates in the experimental design. Adequate replication of the design center point was necessary to avoid distortion particularly in the surface confidence intervals.

Our optimization approach satisfied two criteria. First, sufficient pyrolysis of OC must occur so that unpyrolyzed OC is not measured as native BC after the split point. Second, equivalence must be established between the apparent specific absorption cross sections of OC char and what the instrument determines as native BC. Temperature conditions in the helium phase that satisfied the first criterion were revealed from a σ_{BC} ridge at higher temperatures. The intersection of the response surfaces for σ_{Char} and σ_{BC} revealed the temperature conditions in the helium phase that allowed for the cross sections to be equivalent, thus satisfying the second optimization criterion. Excellent agreement was found between the σ_{BC} ridge and the σ intersection. Moreover, the σ_{BC} ridge fell well within the 95 % confidence region defined by the intersection of the σ_{BC} surface with the 95 % confidence interval surfaces for σ_{Char}. The confidence region revealed a range of acceptable temperatures and durations for the high-temperature step (4) in helium. From the overlap of confidence regions from response surface models of different types of ambient PM2.5, a mechanism exists for converging on a comprehensive TOT temperature protocol. A manuscript on the comprehensive protocol based on this approach is in preparation.

Supporting Information Available

This material is available free of charge at http://pubs.acs.org.

Acknowledgements

The authors would like to thank D. Napier, J. Brown, and E. Edgerton of Atmospheric Research and Analysis, Durham, NC, and S. Biswas, B. Chakrabarti, and C. Sioutas of the Dept. of Civil and Environmental Engineering, Univ. of Southern California, Los Angeles, CA for assistance in collecting samples. In addition, we would like to thank J. J. Filliben of NIST for helpful discussions on the experimental design used in this study. This work was funded by the United States Environmental Protection Agency under interagency agreement (IAG) contract #DW-13-93997301-01 with NIST. Mention of trade names or commercial products does not constitute endorsement or recommendation for use by the U.S. EPA.

Reference List

1. Pope, C. A.; Burnett, R. T.; Thun, M. J.; Calle, E. E.; Krewski, D.; Ito, K.; Thurston, G. D. *Jama-Journal of the American Medical Association* **2002,** *287*, 1132-41.

2. Cormier, S. A.; Lomnicki, S.; Backes, W.; Dellinger, B. *Environmental Health Perspectives* **2006,** *114*, 810-17.

3. Pratsinis, S; Novakov, T.; Ellis, E. C.; Friedlander, S. K. *J.Air Pollution Control Association* **1984,** *34*, 643-50.

4. Malm, W. C.; Sisler, J. F.; Huffman, D.; Eldred, R. A.; Cahill, T. A. *Journal of Geophysical Research-Atmospheres* **1994,** *99*, 1347-70.

5. Jacobson, M. Z. *Nature* **2001,** *409*, 695-97.

6. Climate Change Science Program and Subcommittee on Global Change Research. Our Changing Planet: The U.S. Climate Change Science Program for Fiscal Year 2006. 2006. Washington, DC, U.S. Climate Change Science Program.
Ref Type: Report

7. Yu, H.; Kaufman, Y. J.; Chin, M.; Feingold, G.; Remer, L. A.; Anderson, T. L.; Balkanski, Y.; Bellouin, N.; Boucher, O.; Christopher, S.; DeCola, P.; Kahn, R.; Koch, D.; Loeb, N.; Reddy, M. S.; Schulz, M.; Takemura, T.; Zhou, M. *Atmospheric Chemistry and Physics* **2006,** *6*, 613-66.

8. Birch, M. E.; Cary, R. A. *Analyst* **1996,** *121*, 1183-90.

9. Chow, J. C.; Watson, J. G.; Pritchett, L. C.; Pierson, W. R.; Frazier, C. A.; Purcell, R. G. *Atmospheric Environment Part A-General Topics* **1993,** *27*, 1185-201.

10. Conny, J. M.; Klinedinst, D. B.; Wight, S. A.; Paulsen, J. L. *Aerosol Science and Technology* **2003,** *37*, 703-23.

11. Schauer, J. J.; Mader, B. T.; Deminter, J. T.; Heidemann, G.; Bae, M. S.; Seinfeld, J. H.; Flagan, R. C.; Cary, R. A.; Smith, D.; Huebert, B. J.; Bertram, T.; Howell, S.; Kline, J. T.; Quinn, P.; Bates, T.; Turpin, B.; Lim, H. J.; Yu, J. Z.; Yang, H.; Keywood, M. D. *Environmental Science & Technology* **2003,** *37*, 993-1001.

12. Countess, R. J. *Aerosol Science and Technology* **1990,** *12*, 114-21.

13. Currie L.A.et al. *J.Res.Natl.Inst.Stand.Technol.* **2002,** *107*, 279-98.

14. Hitzenberger, R.; Jennings, S. G.; Larson, S. M.; Dillner, A.; Cachier, H.; Galambos, Z.; Rouc, A.; Spain, T. G. *Atmospheric Environment* **1999,** *33*, 2823-33.

15. Subramanian, R.; Khlystov, A. Y.; Robinson, A. L. *Aerosol Science and Technology* **2006,** *40*, 763-80.

16. Yang, H.; Yu, J. Z. *Environmental Science & Technology* **2002,** *36*, 5199-204.

17. Johnson, R. L.; Shah, J. J.; Cary, R. A.; Huntzicker, J. J. *Atmospheric Aerosol: Source/Air Quality Relationships*, Macias, E. S.; Hopke, P. K., Eds.; American Chemical Society: Washington, D.C., 1981; Chapter 12.

18. Lindberg, J. D.; Douglass, R. E.; Garvey, D. M. *Applied Optics* **1999,** *38*, 2369-76.

19. Clarke, A. D. *Applied Optics* **1982,** *21*, 3011-20.

20. Gorbunov, B.; Hamilton, R.; Hitzenberger, R. *Aerosol Science and Technology* **2002,** *36*, 123-35.

21. Chen, L.-W. A.; Chow, J. C.; Watson, J. G.; Moosmuller, H.; Arnott, P. *Journal of Aerosol Science* **2004,** *35*, 765-80.

22. Subramanian, R.; Roden, C. A.; Boparai, P.; Bond, T. C. *Aerosol Science and Technology* **2007,** *41*, 630-37.

23. Box, G. E. P.; Draper, N. R. *Empirical Model-Building and Response Surfaces,* John Wiley & Sons: New York, 1987.

24. Deming, S. N.; Morgan, S. L. *Experimental Design: A Chemometric Approach,* Elsevier: Amsterdam, 1993.

25. Massart, D. L.; Vandeginste, B. G. M.; Deming, S. N.; Michotte, Y.; Kaufman, L. *Chemometrics: A Textbook,* Elsevier: Amsterdam, 1988.

26. Novakov, T.; Corrigan, C. E. *Mikrochimica Acta* **1995,** *119*, 157-66.

27. Conny, J. M.; Olson, D. A.; Norris, G. A.; Gould, T.; Biswas, S.; Chakrabarti, B.; Sioutas, C. *Journal of Geophysical Research* **2007,** *submitted.*

28. Conny, J. M. The Optimization of Thermal Optical Analysis for the Measurement of Black Carbon in Regional PM2.5: A Chemometric Approach. EPA 600/R-07/119. 8-1-2007. Research Triangle Park, NC, U.S. EPA.
Ref Type: Report

29. Box, G. E. P.; Hunter, W. G.; Hunter, J. S. *Statistics for Experimenters,* John Wiley & Sons: New York, 1978.

30. Gundel, L. A.; Dod, R. L.; Rosen, H.; Novakov, T. *Science of the Total Environment* **1984,** *36*, 197-202.

31. Hansen, A. D. A.; Rosen, H.; Novakov, T. *Science of the Total Environment* **1984,** *36*, 191-96.

32. Rosen, H.; Novakov, T. *Applied Optics* **1983,** *22*, 1265-67.

33. Arnott, W. P.; Hamasha, K; Moosmuller, H.; Sheridan, P. J.; Ogren, J. A. *Aerosol Science and Technology* **2005,** *39*, 17-29.

34. Petzold, A.; Kopp, C.; Niessner, R. *Atmospheric Environment* **1997,** *31*, 661-72.

35. Clarke, A. D. *Applied Optics* **1982,** *21*, 3021-31.

36. Sadler, M; Charlson, R. J.; Rosen, H.; Novakov, T. *Atmospheric Environment* **1981,** *15*, 1265-68.

37. Weingartner, E.; Saathoff, H.; Schnaiter, M.; Streit, N.; Bitnar, B.; Baltensperger, U. *Journal of Aerosol Science* **2003,** *34*, 1445-63.

38. Kirchstetter, T. W.; Novakov, T. *Atmospheric Environment* **2007,** *41*, 1874-88.

39. Yu, J. Z.; Xu, J. H.; Yang, H. *Environmental Science & Technology* **2002,** *36*, 754-61.

40. Birch, M. E. *NIOSH Manual of Analytical Methods (NMAM), DHHS (NIOSH) Publication No. 94-113*, Cassinelli, M. E.; O'Connor, P. F., Eds.; 4th ed.; National Institute for Occupational Safety and Health (NIOSH), US Department of Health and Human Services: Cincinnati, OH, 1999.

41. NAREL. NAREL Standard Operating Procedure Carbon Analysis for the PM2.5 Chemical Speciation QA Program. 11-1-2002. Monitoring and Analytical Services Branch, National Air and Radiation Environmental Laboratory, U.S. EPA Office of Radiation and Indoor Air. 11-1-2002.
Ref Type: Report

42. Turpin, B. J.; Huntzicker, J. J.; Adams, K. M. *Atmospheric Environment Part A-General Topics* **1990,** *24*, 1831-35.

LIST OF FIGURES

Figure 7. BC/TC response surfaces as a function of He step-4 temperature and duration and using the central condition of Factor 3 (550 °C temperature step ramp). (a) level-1 sample; (b) level-2 sample. Also shown are the 95 % confidence interval surfaces.

Figure 8. 3D scatter plots of σ_{Char} (a) and σ_{BC} (b) vs. He step-4 temperature and duration for the level-1 sample. Shaded circles indicate measurements from the full factorial, open circles indicate measurements from the partial factorial (Fig. 2). Arrows indicate standard deviation for replicate measurements.

Figure 9. Overlay of the σ_{BC} and σ_{Char} surfaces for the level-1 (a) and level-2 (b) samples. OC Char is pyrolyzed OC. Surfaces for the level-2 sample are bracketed by 95 % confidence intervals. Confidence intervals for the level-1 sample (omitted for clarity) are comparable to those for the level-2 sample.

Figure 10. Variation in σ_{Char} and σ_{BC} with total carbon for all samples collected at the Seattle site. Points (1) and (2) indicate data for the level-1 and level-2 samples, respectively.

Figure 11. Comparison of σ_{BC} surfaces for the level-1 and level-2 samples. OC Char is pyrolyzed OC.

Figure 12. Variation in the σ_{Char} (a) and σ_{BC} (b) surfaces for the level-1 sample at five temperature ramps in the O_2-He phase, which correspond to levels of Factor 3 in the factorial design.

Figure 13. (a) Overhead view of the overlay of σ_{Char} (light) and σ_{BC} (dark) surfaces for the level-1 sample from Fig. 12 a. (b) Two-dimensional projection of the 95 % confidence region (see

text) and the σ intersection for the level-1 sample, ridges of σ_{BC} maxima for both samples, and the BC/TC minimum for the level-2 sample.

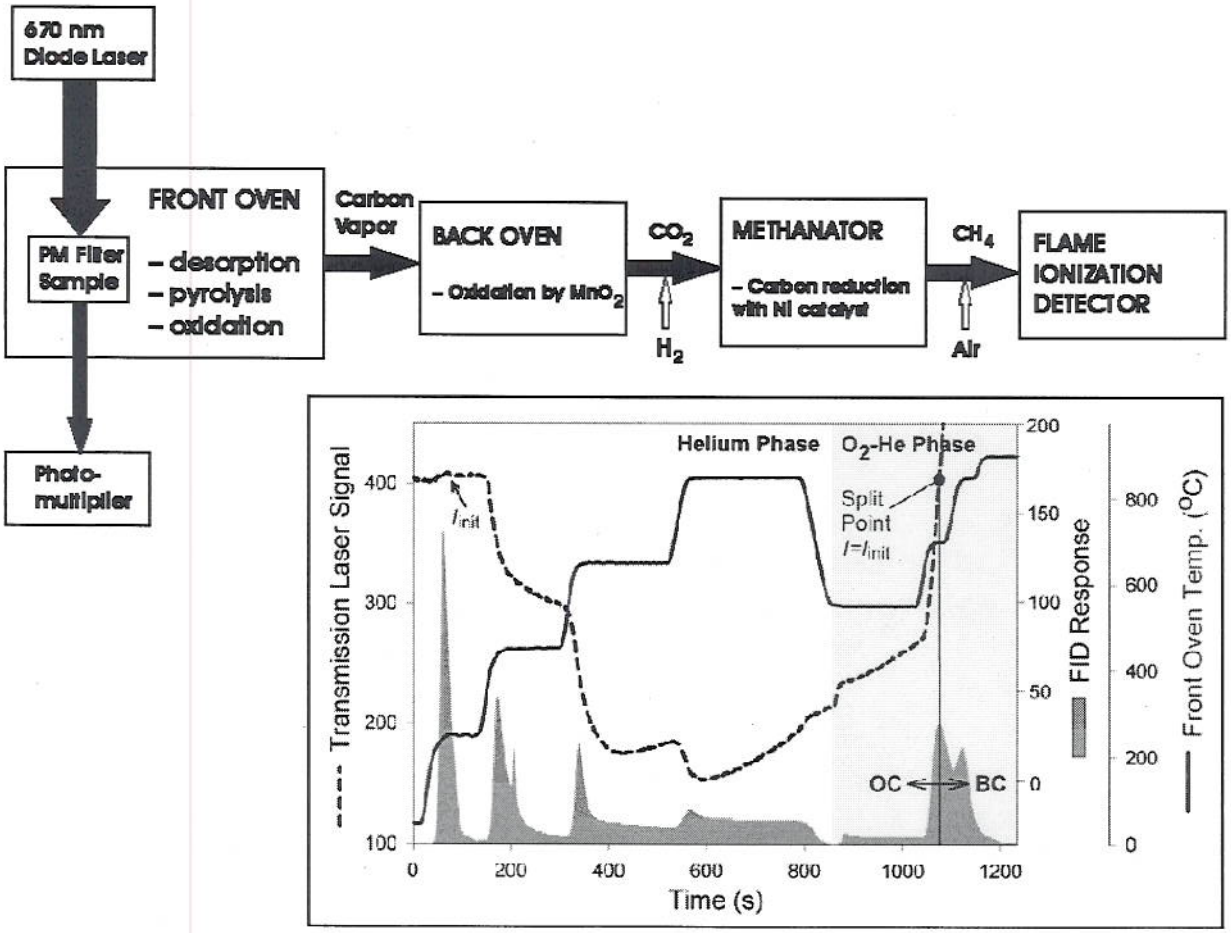
670 nm
Diode Laser
FRONT OVEN
PM Filter
Sample
– desorption
– pyrolysis
– oxidation
Carbon
Vapor
BACK OVEN
– Oxidation by MnO_2
CO_2
H_2
METHANATOR
– Carbon reduction
with Ni catalyst
CH_4
Air
FLAME
IONIZATION
DETECTOR
Photo-
multiplier
Helium Phase
O_2-He Phase
Split
Point
$I=I_{init}$
I_{init}
OC
BC
Transmission Laser Signal
FID Response
Front Oven Temp. (°C)
Time (s)

Figure 1

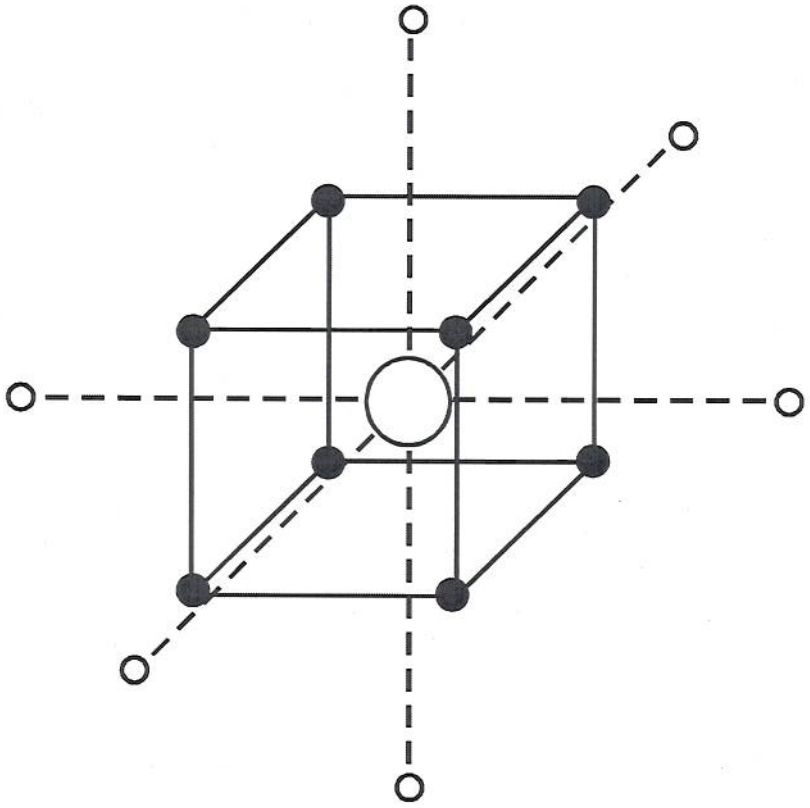

Figure 2

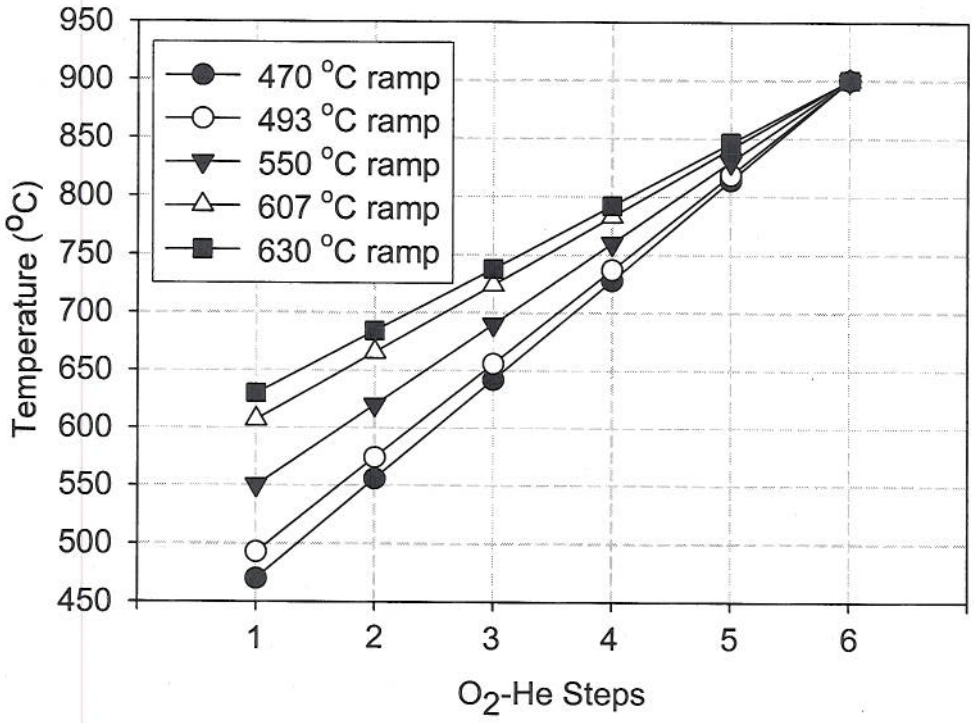
950
900
850
800
750
700
650
600
550
500
450
Temperature (°C)
470 °C ramp
493 °C ramp
550 °C ramp
607 °C ramp
630 °C ramp
1
2
3
4
5
6
O2-He Steps

Figure 3

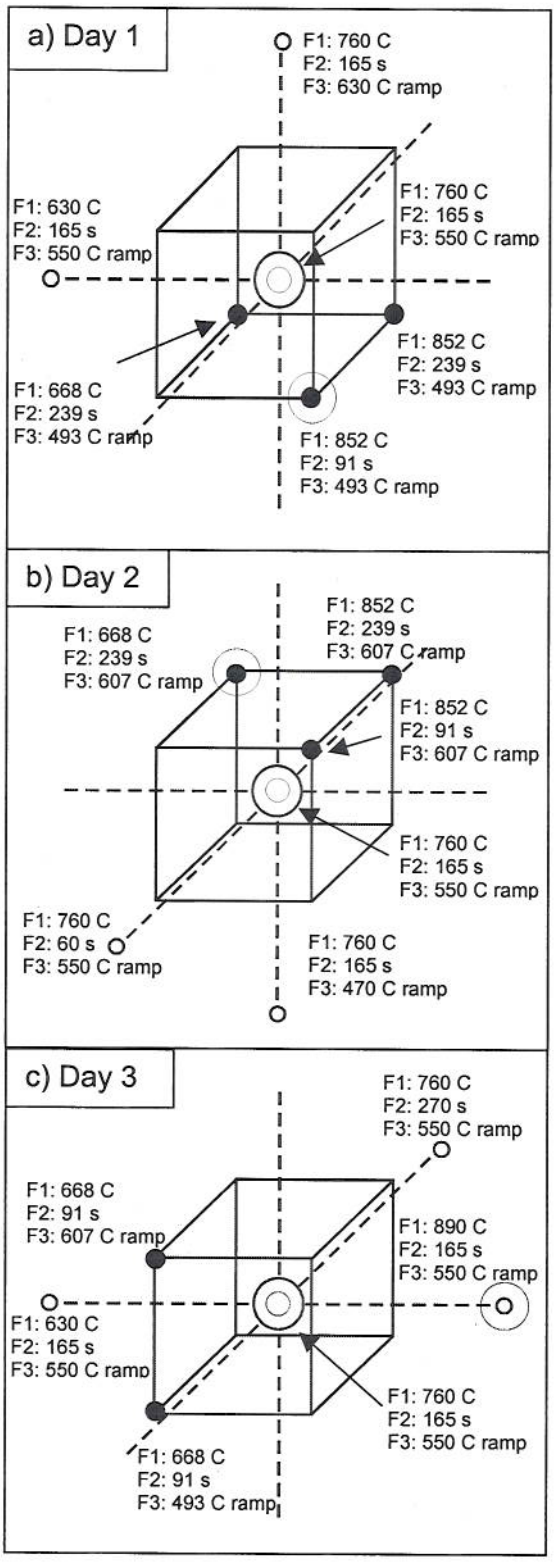
a) Day 1
F1: 760 C
F2: 165 s
F3: 630 C ramp
F1: 630 C
F2: 165 s
F3: 550 C ramp
F1: 760 C
F2: 165 s
F3: 550 C ramp
F1: 852 C
F2: 239 s
F3: 493 C ramp
F1: 668 C
F2: 239 s
F3: 493 C ramp
F1: 852 C
F2: 91 s
F3: 493 C ramp
b) Day 2
F1: 852 C
F2: 239 s
F3: 607 C ramp
F1: 668 C
F2: 239 s
F3: 607 C ramp
F1: 852 C
F2: 91 s
F3: 607 C ramp
F1: 760 C
F2: 165 s
F3: 550 C ramp
F1: 760 C
F2: 60 s
F3: 550 C ramp
F1: 760 C
F2: 165 s
F3: 470 C ramp
c) Day 3
F1: 760 C
F2: 270 s
F3: 550 C ramp
F1: 668 C
F2: 91 s
F3: 607 C ramp
F1: 890 C
F2: 165 s
F3: 550 C ramp
F1: 630 C
F2: 165 s
F3: 550 C ramp
F1: 760 C
F2: 165 s
F3: 550 C ramp
F1: 668 C
F2: 91 s
F3: 493 C ramp

Figure 4

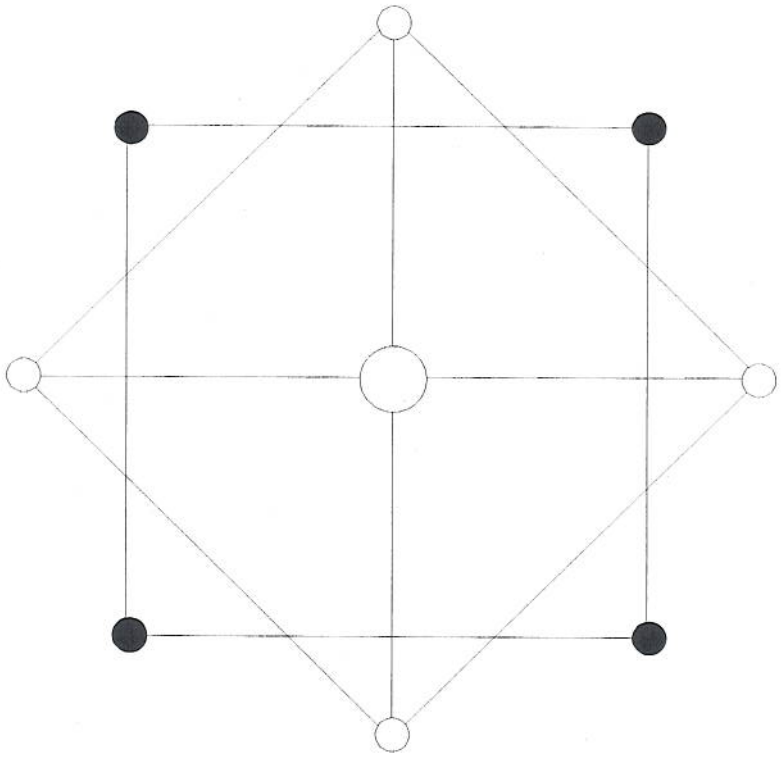

Figure 5

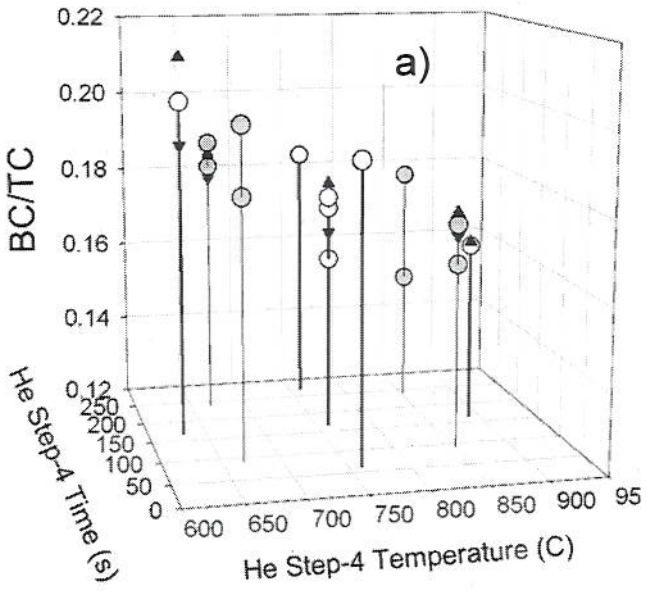
a)
BC/TC
0.22
0.20
0.18
0.16
0.14
0.12
He Step-4 Time (s)
250
200
150
100
50
0
600
650
700
750
800
850
900
95
He Step-4 Temperature (C)

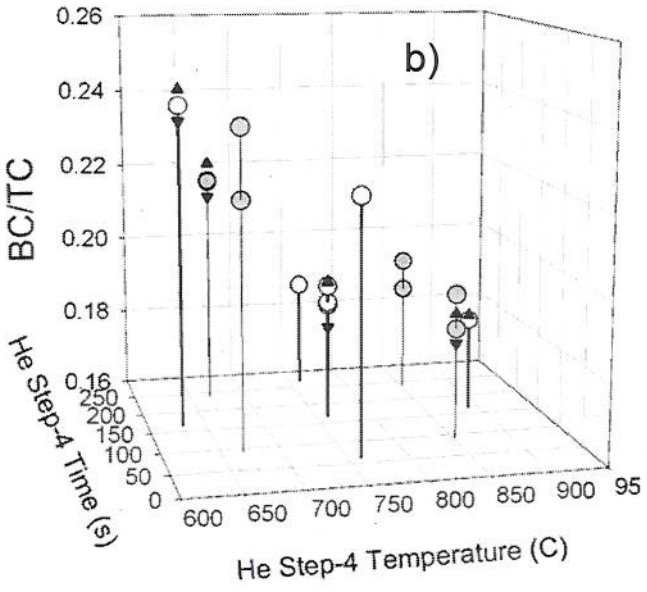
b)
BC/TC
0.26
0.24
0.22
0.20
0.18
0.16
He Step-4 Time (s)
250
200
150
100
50
0
600
650
700
750
800
850
900
95
He Step-4 Temperature (C)

Figure 6

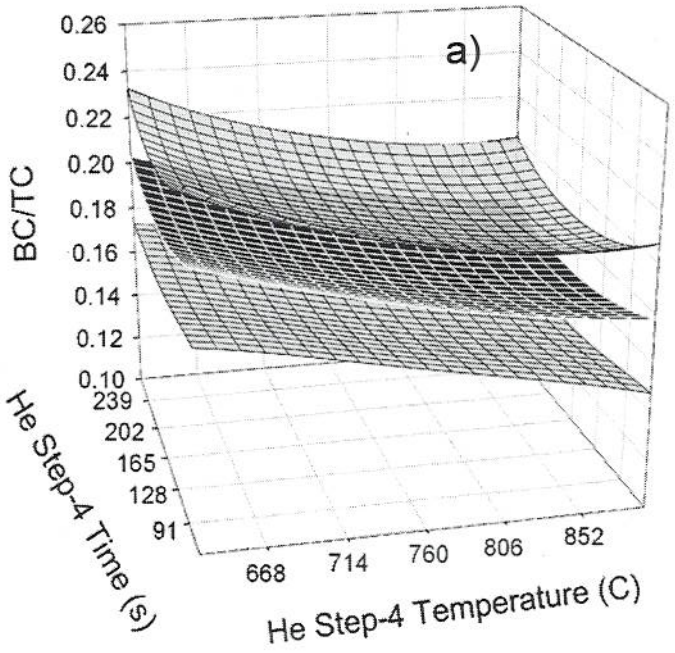
a)
BC/TC
0.26
0.24
0.22
0.20
0.18
0.16
0.14
0.12
0.10
He Step-4 Time (s)
239
202
165
128
91
668
714
760
806
852
He Step-4 Temperature (C)

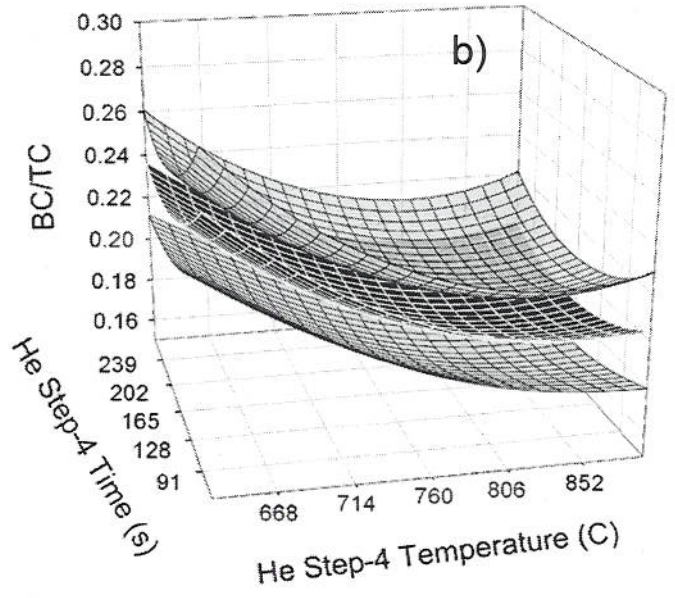
b)
BC/TC
0.30
0.28
0.26
0.24
0.22
0.20
0.18
0.16
He Step-4 Time (s)
239
202
165
128
91
668
714
760
806
852
He Step-4 Temperature (C)

Figure 7

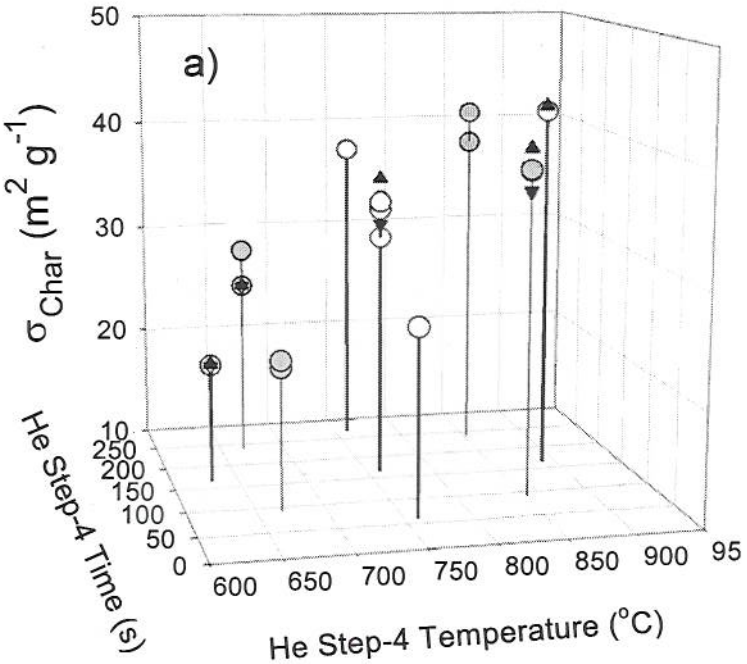
a)
σChar (m2 g-1)
50
40
30
20
10
He Step-4 Time (s)
250
200
150
100
50
0
600
650
700
750
800
850
900
95
He Step-4 Temperature (°C)

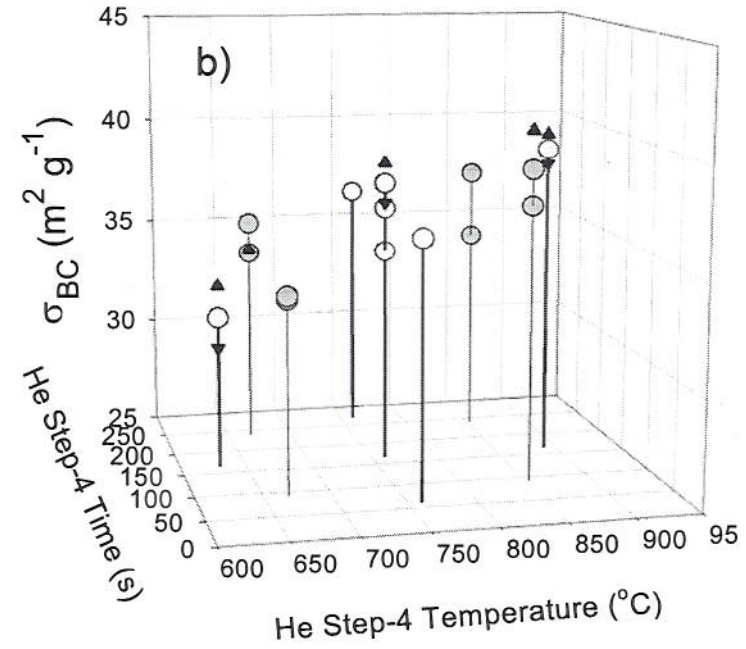
b)
σBC (m2 g-1)
45
40
35
30
25
He Step-4 Time (s)
250
200
150
100
50
0
600
650
700
750
800
850
900
95
He Step-4 Temperature (°C)

Figure 8

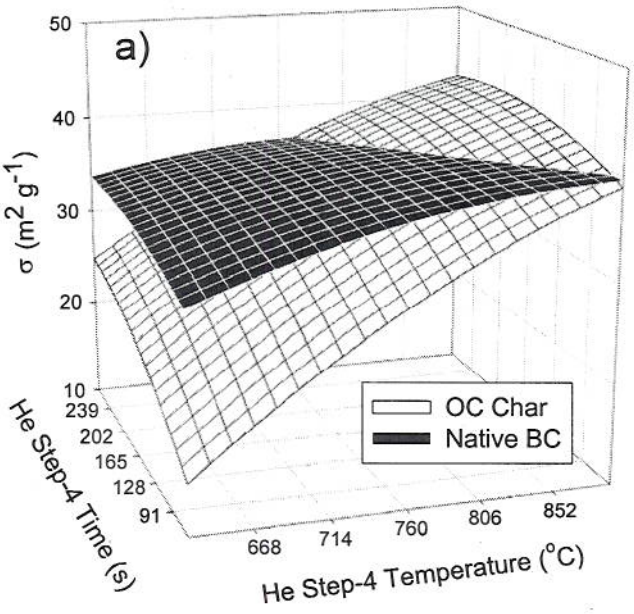
a)
σ (m2 g-1)
50
40
30
20
10
He Step-4 Time (s)
239
202
165
128
91
668
714
760
806
852
He Step-4 Temperature (°C)
OC Char
Native BC

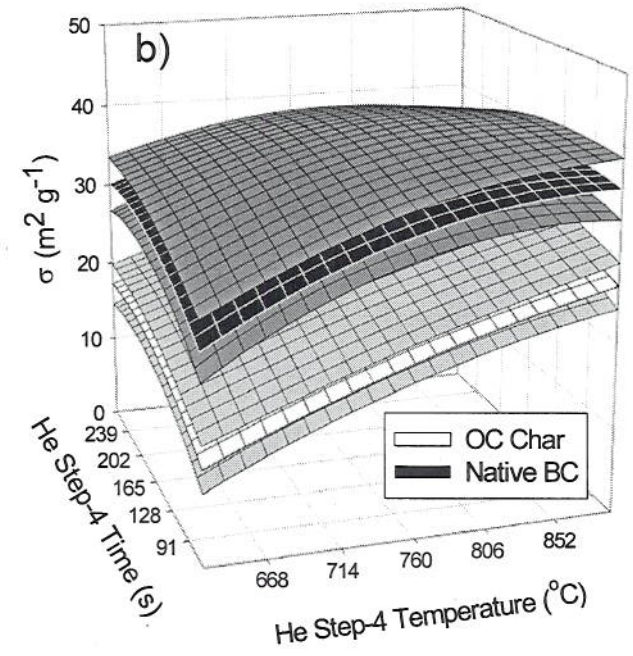
b)
σ (m2 g-1)
50
40
30
20
10
0
He Step-4 Time (s)
239
202
165
128
91
668
714
760
806
852
He Step-4 Temperature (°C)
OC Char
Native BC

Figure 9

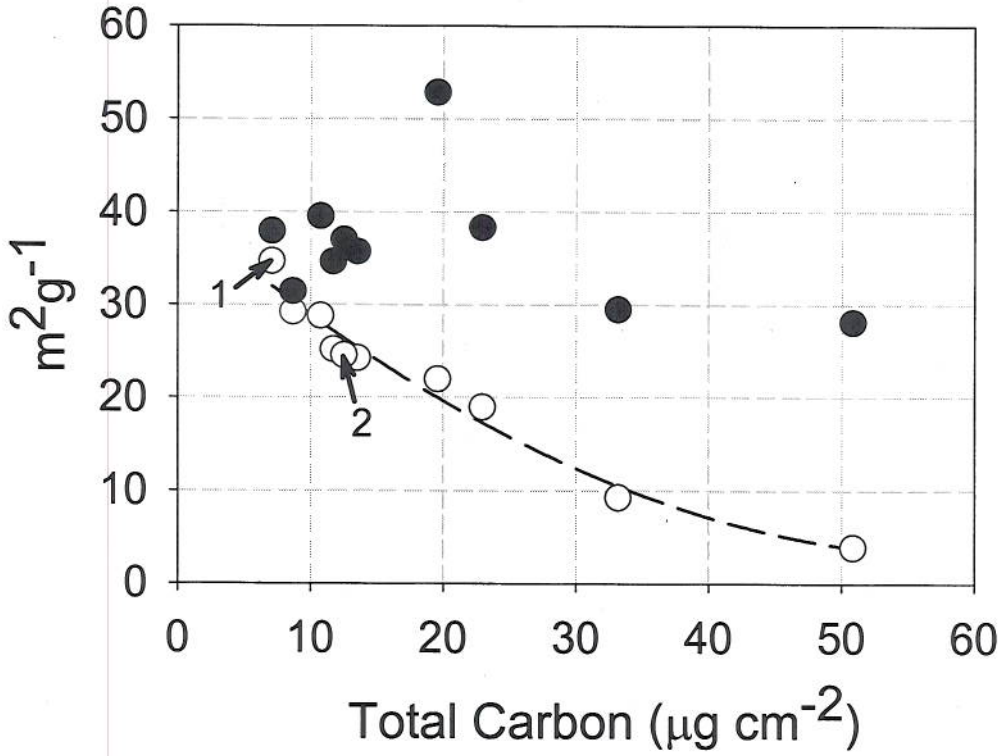

Figure 10

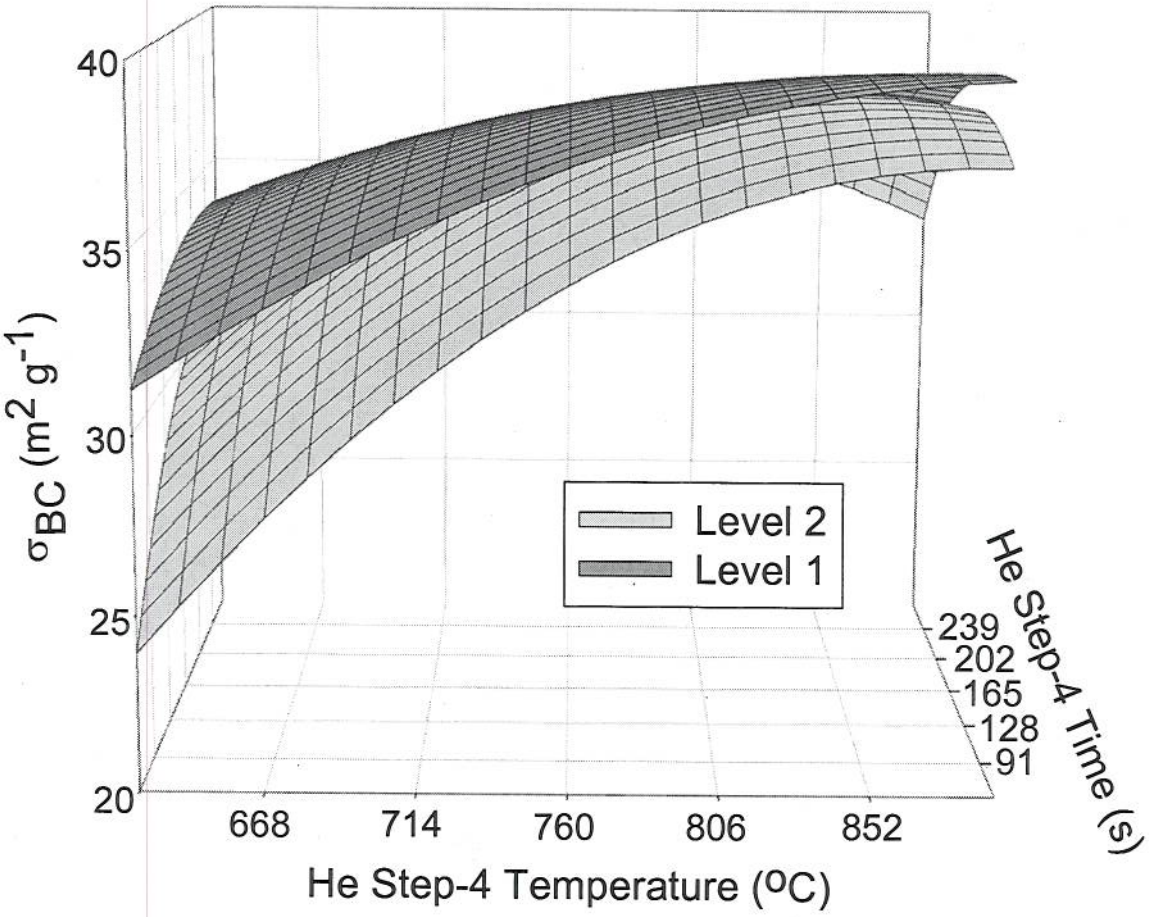
40
35
30
25
20
σBC (m2 g-1)
Level 2
Level 1
239
202
165
128
91
He Step-4 Time (s)
668
714
760
806
852
He Step-4 Temperature (oC)

Figure 11

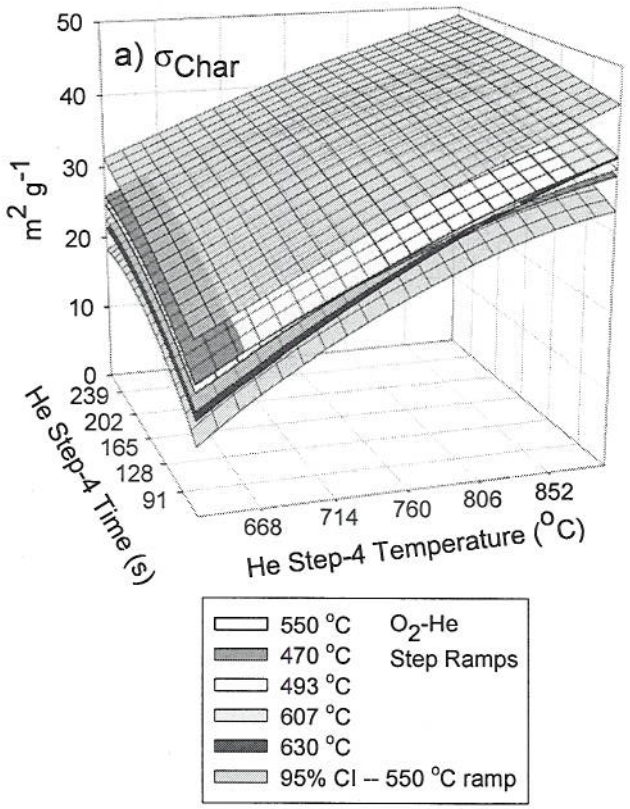
a) σChar
50
40
30
20
10
0
m2 g-1
He Step-4 Time (s)
239
202
165
128
91
668
714
760
806
852
He Step-4 Temperature (°C)
550 °C
470 °C
493 °C
607 °C
630 °C
95% CI -- 550 °C ramp
O2-He
Step Ramps

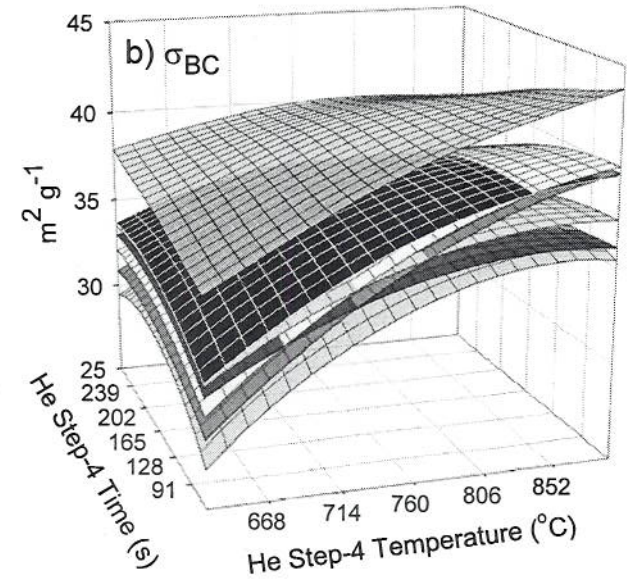
b) σBC
45
40
35
30
25
m2 g-1
He Step-4 Time (s)
239
202
165
128
91
668
714
760
806
852
He Step-4 Temperature (°C)

Figure 12

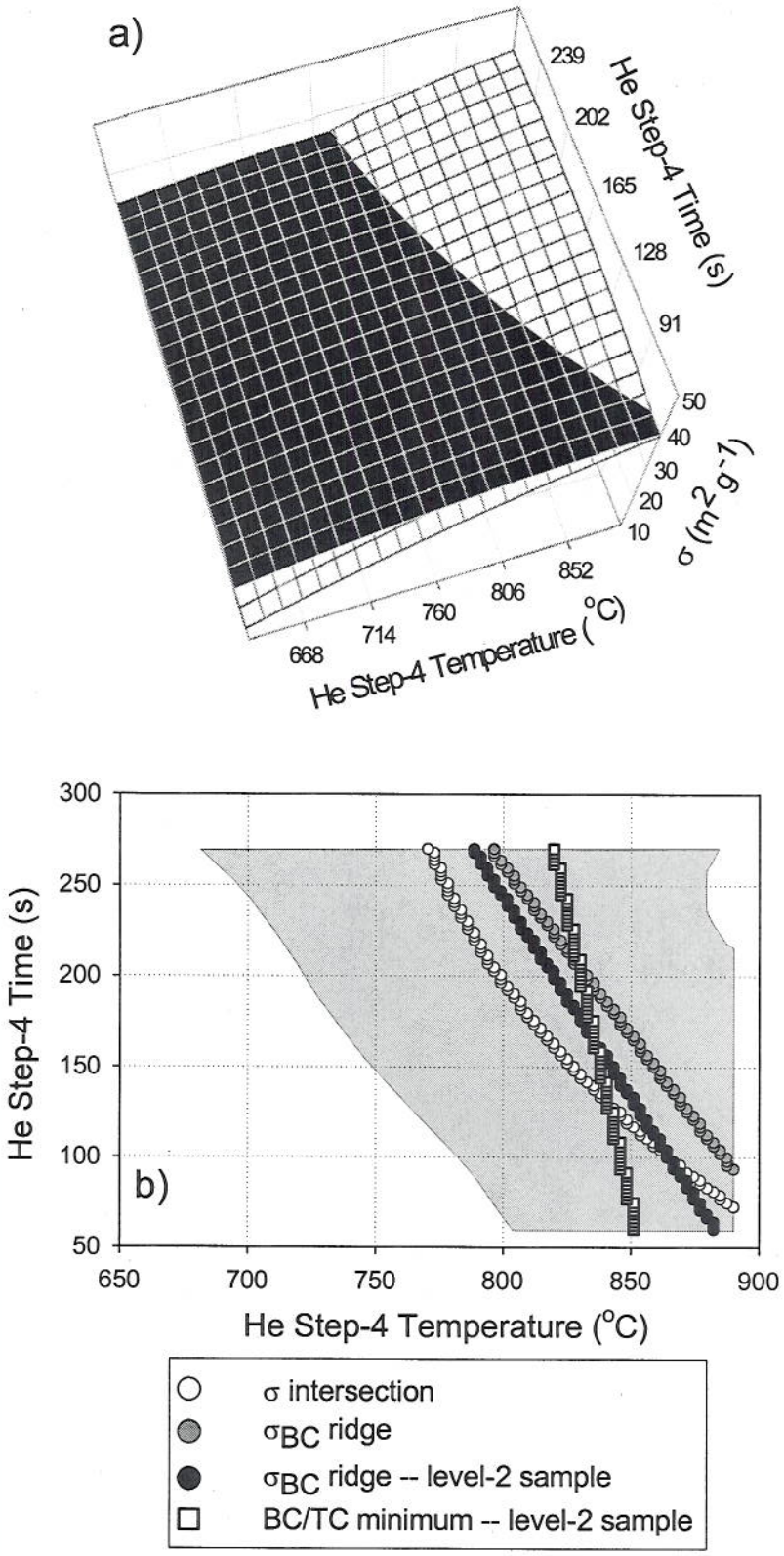
a)
239
202
165
128
91
50
He Step-4 Time (s)
40
30
20
10
σ (m^2 g^-1)
852
806
760
714
668
He Step-4 Temperature (°C)
b)
300
250
200
150
100
50
He Step-4 Time (s)
650
700
750
800
850
900
He Step-4 Temperature (°C)
σ intersection
σBC ridge
σBC ridge -- level-2 sample
BC/TC minimum -- level-2 sample

Figure 13

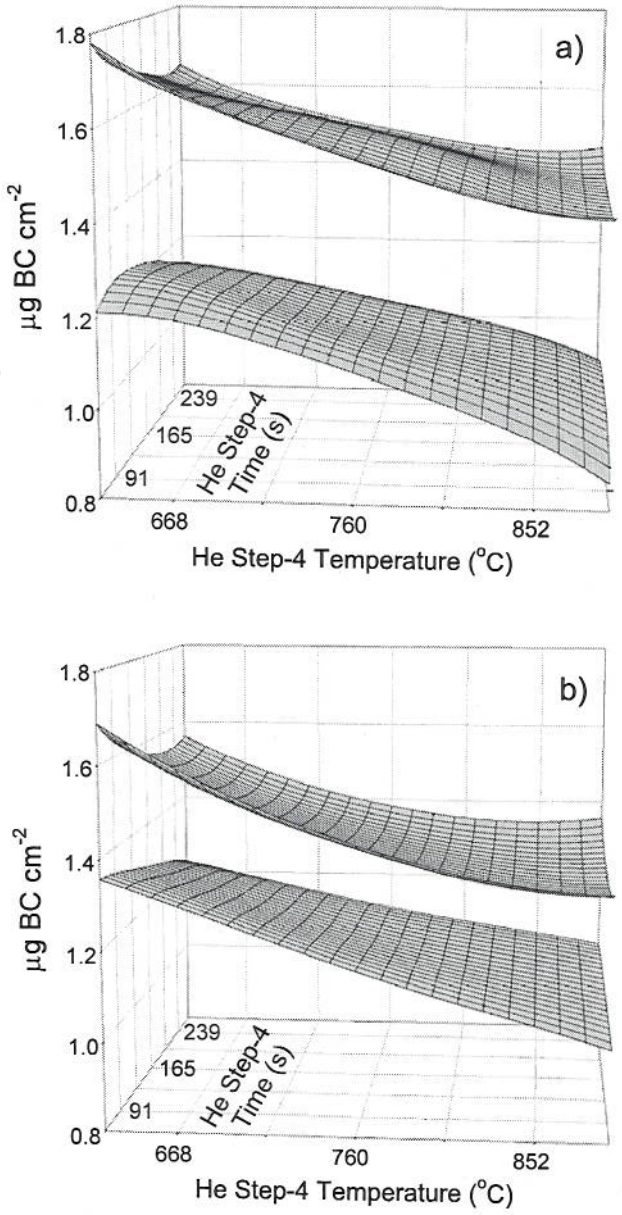

Figure S1. 95 % confidence interval surfaces for the BC concentration model without factorial center point replication (a) and with 6x replication (b) in the experimental design. Inadequate center point replication causes the confidence interval surfaces to widen and become distorted as evidenced by the bulge at the center of the upper surface in (a).

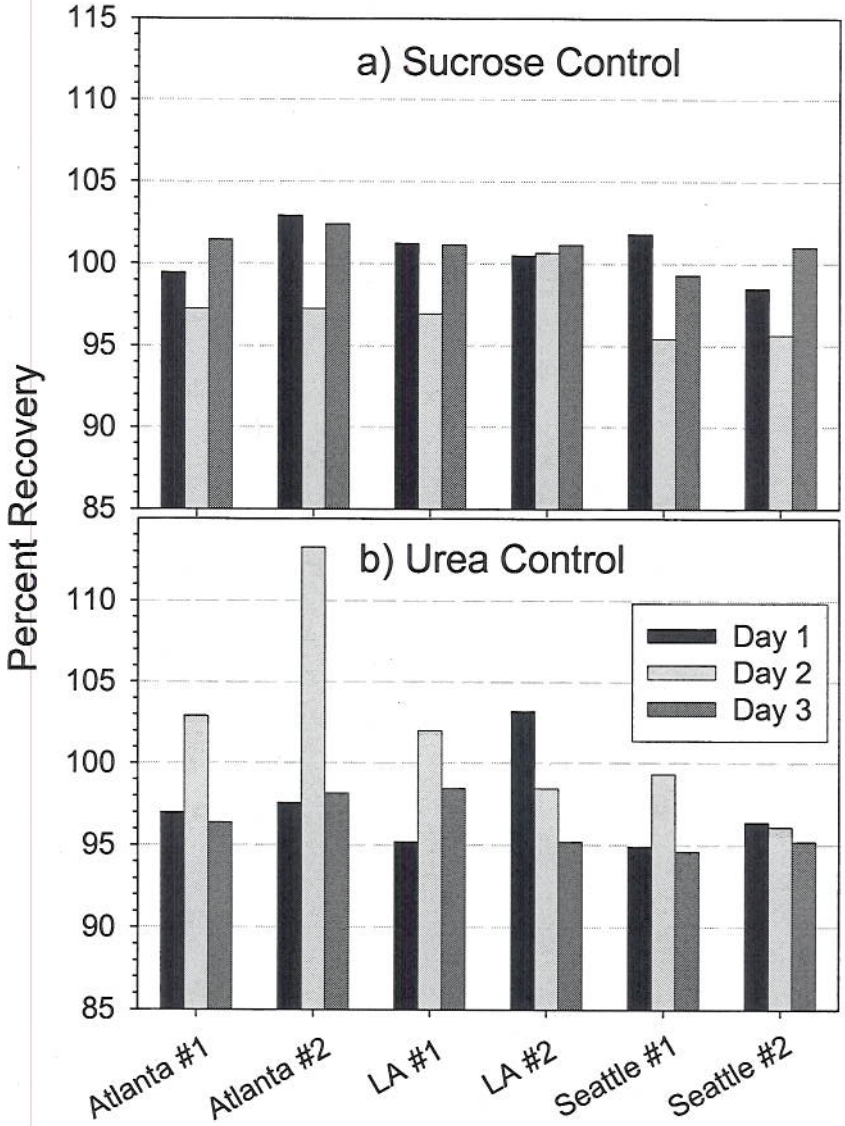

Figure S2. Percent recoveries of sucrose (a) and urea (b) controls for two selected samples each from sampling sites in Atlanta and Los Angeles as well as the two samples used in modeling from the Seattle site. The sucrose control with higher carbon was run at the beginning of analysis days 1 and 3 and at the end of day 2. The urea control with lower carbon was run at the beginning of day 2 and at the end of days 1 and 3. Result showed that measurement drift occurred regardless of the type of compound or carbon concentration.

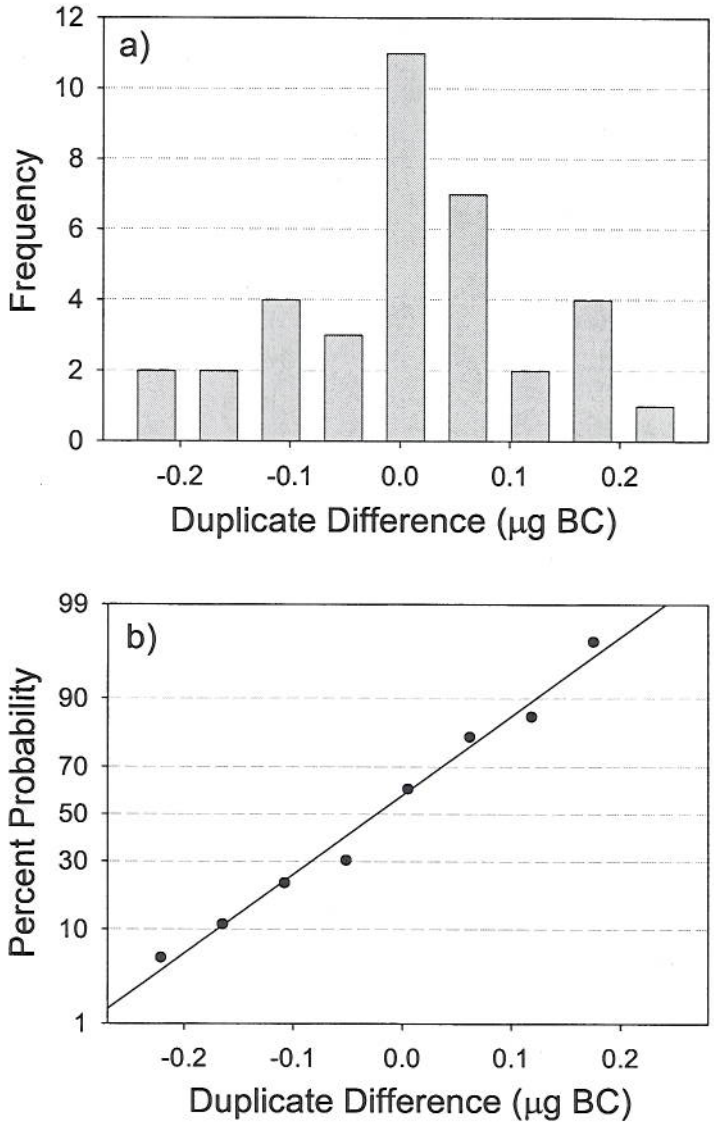

Figure S3. Differences in the BC determinations for within-day duplicated points in the factorial design. (a) frequency distribution; (b) cumulative frequencies vs. percent probability. Data are from four ancillary samples (two each from Atlanta and Los Angeles) in addition to the two Seattle samples used in modeling. Duplicate measurements were made at six points in the design for each sample. Results show that BC differences are normally distributed.

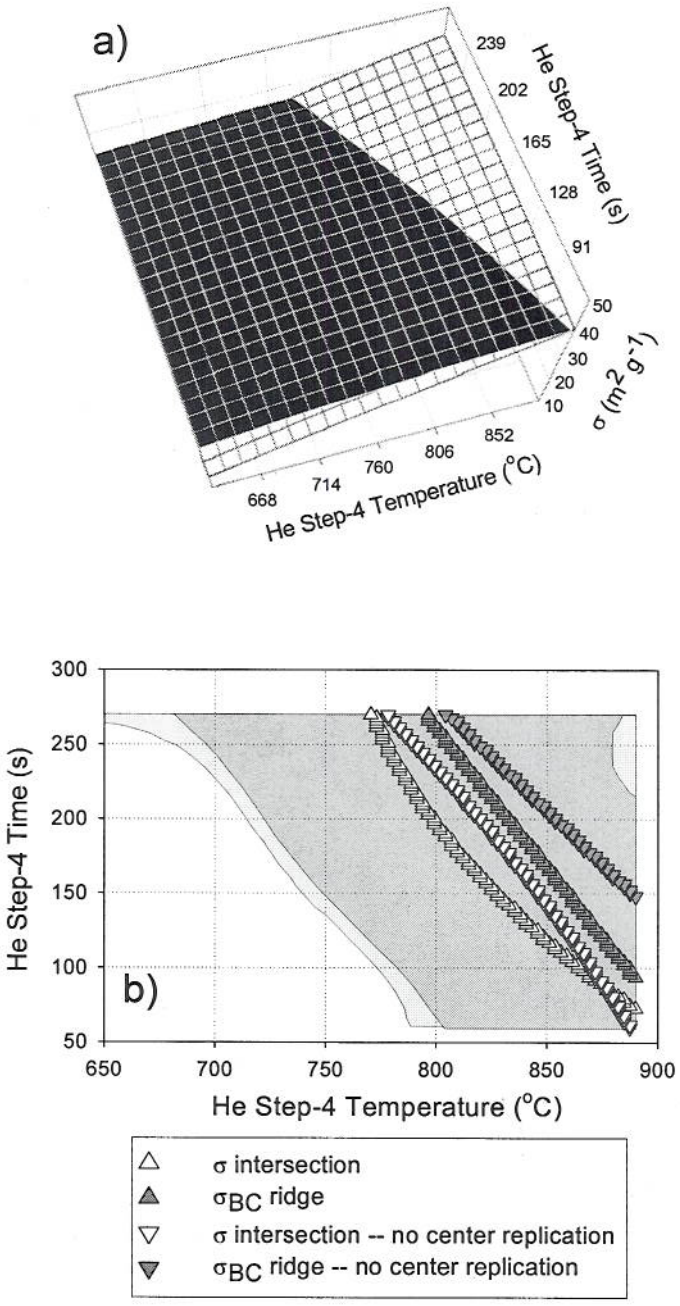

Figure S4. Projections of σ response surfaces for the experiment without replication of the factorial center point. (a) Overhead view of the overlay of σ_{Char} and σ_{BC} surfaces for the level-1 sample. (b) Two-dimensional projection of the 95 % confidence region (light shaded area), the σ

intersection, and the σ_{BC} ridge for the level-1 sample. The confidence region for the experiment with center point replication (dark shaded area) and the σ_{BC} ridge for this case are shown for comparison. In (a), note the slight difference in the shape of the σ intersection for the level-1 sample compared to that in Fig. 13a. In (b), the 95 % confidence region for the level-1 sample is clearly larger when the center point is not replicated. In addition, both the σ intersection and the σ_{BC} ridge are shifted to higher step-4 temperatures. For example, the σ intersection at 150 s is shifted 17 °C higher when there is no center point replication.